Chemical Engineering Science 277 (2023) 118828

Contents lists available at ScienceDirect

Chemical Engineering Science

journal homepage: www.elsevier.com/locate/ces

Interface mass transfer and properties of bubbly flows in a column with Newtonian and non-Newtonian liquids

Ida K. Kure *, Hugo A. Jakobsen, Jannike Solsvik *

Department of Chemical Engineering, Norwegian University of Science and Technology (NTNU), N-7491 Trondheim, Norway

ARTICLE INFO

Keywords:
Bubble column
Mass transfer
Bubble clusters
Rheology
Shadow imaging
Image analysis
Bubble size

ABSTRACT

The mass transfer of gas–liquid systems is commonly reported through the volumetric mass transfer coefficient, $k_L a$, which is a function of several complex phenomena. To optimize the rate of mass transfer, increased knowledge about the individual effects of the interfacial area, a, and the liquid-side mass transfer coefficient, k_L, on $k_L a$ is necessary. In this study, $k_L a$ was measured by monitoring the dissolved oxygen concentration in a bubble column. The bubble flows were recorded by a photographic method and the images were analyzed by means of artificial neural network to determine the bubble size. The effects of rheology, superficial gas velocity, and gas sparger design were analyzed. k_L decreased with an increase in the superficial gas velocity and with an increase in the viscosity. The relative change in a was much larger compared to the relative change in k_L, and hence, for the investigated operational conditions and liquid solutions, the change in $k_L a$ was mainly attributed to the change in a. Bubble clusters were formed in the non-Newtonian solutions but for the given operating conditions and liquid solutions, the bubble cluster formation did not have a prominent effect on the mass transfer.

1. Introduction

Interfacial mass transfer is an important phenomenon influencing a variety of industrial processes involving gas-liquid or gas-liquid-solid interactions, e.g., distillation, waste-water treatment, and chemical and biochemical reactors. Optimizing these processes requires accurate knowledge and data about the transfer of mass across the phase boundaries.

The rate of mass transfer is proportional to the concentration difference between the phases, where the proportionality constant is the volumetric mass transfer coefficient, $k_L a$. Existing works on gas-liquid mass transfer have mainly focused on determining $k_L a$ in bubble swarms (Akita and Yoshida, 1973; Muroyama et al., 2013; Scargiali et al., 2010; Vandu et al., 2004; Zednikova et al., 2018). Complex phenomena are involved in the liquid-side mass transfer coefficient, k_L, and the interfacial area, a. The individual effect of k_L and a on the mass transfer cannot easily be predicted when lumped into the combined coefficient of $k_L a$. Relatively few studies exist where k_L and a have been individually determined in bubble columns (Akita and Yoshida, 1974; Bouaifi et al., 2001; Eckenfelder and Barnhart, 1961; Jeng et al., 1986; Kawase and Moo-Young, 1990; Koide et al., 1985; Miller, 1983; Sastaravet et al., 2020; Vasconcelos et al., 2003). Relevant studies on k_L and a in bubble columns where the latter is determined using a photographic method (Bouaifi et al., 2001; Koide et al., 1985; Sastaravet et al., 2020; Vasconcelos et al., 2003) are summarized in the following.

Koide et al. (1985) and Vasconcelos et al. (2003) studied the influence of anti-foaming agents on $k_L a$, k_L, and a. Koide et al. (1985) performed experiments in water and aqueous solutions of alcohols, while the work of Vasconcelos et al. (2003) was restricted to water. Both Koide et al. (1985) and Vasconcelos et al. (2003) found that $k_L a$ and k_L decreased with presence of anti-foaming agents. Koide et al. (1985) observed that k_L decreased and the gas hold-up, α_G, increased with presence of surfactants (n-alcohols). Furthermore, α_G decreased with presence of anti-foaming agents. Bubble size distributions were not provided in the studies of Vasconcelos et al. (2003) and Koide et al. (1985). Sastaravet et al. (2020) investigated the effect of solid particles on bubble hydrodynamics and mass transfer enhancement in tap water. $k_L a$ increased with increasing superficial gas velocity, u_s, for all conditions, where the presence of solid particles enhanced $k_L a$. k_L decreased with an increase in u_s ($u_s \in [0.26, 1.53]$ cm/s) both with and without solid particles. The bubble sizes with solid particles were reported smaller than without particles (~ 22–27% on average). However,

* Corresponding authors.
E-mail addresses: ida.k.kure@ntnu.no (I.K. Kure), jannike.solsvik@ntnu.no (J. Solsvik).

https://doi.org/10.1016/j.ces.2023.118828
Received 19 September 2022; Received in revised form 17 November 2022; Accepted 29 April 2023
Available online 8 May 2023

in none of the studies the bubble size distributions from which the average bubble diameters were calculated were provided. Considering the splitting of $k_L a$ into k_L and a, it is desirable to have a narrow bubble size distribution from which the mean bubble diameter is calculated. A narrow bubble size distribution increases the accuracy of the influence of a on $k_L a$. Furthermore, in mass transfer studies where k_L is calculated from $k_L a$ and a, reducing the uncertainty in a reduces the uncertainty in k_L. Therefore, when studying the individual effects of k_L and a on $k_L a$, the information of bubble size distributions is necessary. Bouaifi et al. (2001) measured k_L in tap water where air was dispersed through spargers of various designs (membrane, porous plate, and perforated plate). $k_L a$ increased with increasing u_s at all the operating conditions. k_L was independent of the specific power consumption which was related to the gas pressure drop – a function of u_s, the sparger pressure drop, the liquid density, gravity, and tank liquid height. Bubble size distributions for the different spargers were provided, where the size distributions ranged from 1.5–6.5 mm and 1.5–6.5 mm for the porous plate and membrane, respectively, and the size distribution ranged from 1.5–11.5 for the perforated plate. For the membrane, approximately 80% of the bubble sizes were within the 3.5–4.5 mm size range.

Despite the analysis of the individual parameters of k_L and a, the experimental data obtained by Koide et al. (1985), Vasconcelos et al. (2003), Sastaravet et al. (2020), and Bouaifi et al. (2001) are limited to Newtonian solutions. In bioprocesses, e.g., in fermentation, the viscosity of the fermentation fluids is affected by the presence of cells, substrates, and products (Doran, 2013). A variety of fermentation processes involve materials that exhibit non-Newtonian behavior (Badino et al., 1976; Blanch and Bhavaraju, 1976), e.g., culture broths with suspended cells and extracellular polysaccharides (Doran, 2013). The non-Newtonian fluids commonly found in bioprocesses are pseudoplastic, Bingham plastic, and Casson plastic (Doran, 2013). Motivated by industrial application, the study of the individual contributions of k_L and a to $k_L a$ should be extended from Newtonian solutions to viscous Newtonian and non-Newtonian solutions.

Augier and Raimundo (2021) studied the effect of rheology on mass transfer and bubble size in bubbly flows in the heterogeneous regime ($u_s \in [3, 30]$ cm/s). k_L, a, and local gas volume fraction were measured in non-Newtonian solutions (carboxymethyl cellulose (CMC) and xanthan gum (XG)). The gas was dispersed by a perforated plate which was chosen similar to that of Gemello et al. (2018), which enabled generation of bubbles in water that were close to their initial size. An in-situ probe (referred to as cross-correlation method) was applied to measure the bubble size and the local gas volume fraction. The differences in the measured bubble size between the solutions were governed by the rheology and not u_s. Except in water, where u_s had a strong effect on k_L, the rheology of the solutions explained the differences in the measured k_L. $k_L a$ and the local gas volume fraction were governed by both the rheology and u_s. The summarized results by Augier and Raimundo (2021) are based on radially averaged values of the bubble size and the local gas volume fraction. For $u_s > 3$ cm/s, the bubble diameter varied with the radial position. Bubble size distributions were not provided, and with a variation in the bubble diameter and the local gas volume with the radial position it is challenging to evaluate the accuracy in k_L when k_L is calculated from a and $k_L a$.

Martínez-Mercado et al. (2007) and Vélez-Cordero and Zenit (2011) developed experimental set-ups which allowed for production of close to mono-sized (narrow bubble size distribution) bubbles. The experimental set-ups were used for studies on bubbly flows in Newtonian (Martínez-Mercado et al. (2007), Vélez-Cordero and Zenit (2011)) and non-Newtonian (Vélez-Cordero and Zenit (2011), Vélez-Cordero et al. (2012)) solutions. With the ability of creating mono-sized bubbles, the design of the experimental set-ups has thus a potential to be further used for accurate mass transfer studies where $k_L a$ is split into k_L and a. Martínez-Mercado et al. (2007) measured the gas and liquid velocities in water and water/glycerol solutions, where the gas was introduced by an array of capillaries which created a mono-sized bubbly flow. The measurements were conducted for bubble Reynolds numbers from 10 to 500. The mean bubble velocity decreased with increasing α_G. For very dilute flows, the measured mean bubble velocity deviated largely from the velocity of a single isolated bubble. Vélez-Cordero and Zenit (2011) studied bubbly flows in the homogeneous regime ($u_s \in [0.09, 0.6]$ cm/s), using XG and glycerol/water solutions. The bubble column was similar to that used by Martínez-Mercado et al. (2007), where sets of capillary banks were designed to create mono-sized bubbles. Bubble clusters (aggregates of bubbles) were only formed in the shear-thinning liquids, where the clusters grew with increased gas volume fraction. Compared to single bubbles, the mean bubble velocity of the clusters increased. During bubble ascent, the bubble clusters had a dynamic structure, rising in the center and descending on the exterior part of the cluster. In some of the shear-thinning solutions, only the smallest bubbles formed clusters. Vélez-Cordero et al. (2012) studied the properties of bubbly flows in elastic fluids with approximately constant viscosity. The bubble column was similar to that by Martínez-Mercado et al. (2007), and the capillary banks were similar to those used by Vélez-Cordero and Zenit (2011). The bubble dispersion changed as function of the bubble size. For smaller bubble diameters, large vertical bubble clusters were formed. The larger bubbles, on the other hand, ascended in a dispersed manner. Although mass transfer analyzes were not performed, Vélez-Cordero et al. (2012) suggested that the formation of small bubbles may not be optimal to achieve high mass transfer rates in visco-elastic flows due to the formation of bubble clusters. Hence, larger bubble sizes could be more convenient for the mass transfer. A next step in the investigations of bubbly flows by Martínez-Mercado et al. (2007); Vélez-Cordero and Zenit (2011), and Vélez-Cordero et al. (2012) is to include mass transfer studies.

The objective of this work was to study the effect of liquid rheology and operating conditions on the mass transfer in a bubble column which enabled the generation of mono-sized bubbles. Due to the complex phenomena involved in $k_L a$, it was of desire to evaluate the individual effects of k_L and a. When splitting $k_L a$ into k_L and a, d_b should be based on a narrow bubble size distribution. A column and sparger design similar to those described by Vélez-Cordero and Zenit (2011) were thus applied to enable production of bubbles with a narrow bubble size distribution. For each sparger used in the present work, bubble size distributions were provided at different u_s and liquid solutions. The oxygen concentration and the bubble sizes were obtained using in situ dissolved oxygen (DO) probes and a high-speed camera. An artificial neural network (ANN) was used in the image processing procedure to determine the bubble sizes with a small statistical uncertainty. The individual effects of k_L and a on $k_L a$ were studied for $u_s \in [0.07, 0.47]$ cm/s. Bubble clusters can be seen in fluids represented in the bioprocess industry. The existing literature on bubble clusters mainly focuses on bubble cluster formation and bubble cluster velocity (Vélez-Cordero and Zenit, 2011). With the increasing interest for bioprocess industry, it is crucial to establish understanding of the mass transfer from bubble clusters for optimal process performance. In this work, the effects of bubble clusters on $k_L a$ and flow dynamics were investigated.

2. Materials and methods

2.1. Experimental setup

The bubble experiments were carried out in a vertical rectangular column with dimensions $180 \times 10 \times 5$ cm^3, as illustrated in Fig. 2.1. The column was made of stainless steel except from the two widest walls which were made of soda-lime glass. The column was mounted to a gas chamber with dimensions $11 \times 10 \times 5$ cm^3 from where the gas phase was dispersed by a capillary bank. Different mean bubble sizes were generated using three capillary banks which were made of stainless steel, noted here as N1, N2, and N3, and which differed in the number of capillaries and their inner diameter. The capillary banks, illustrated in Fig. 2.2 (a), were designed similar to those in the work by

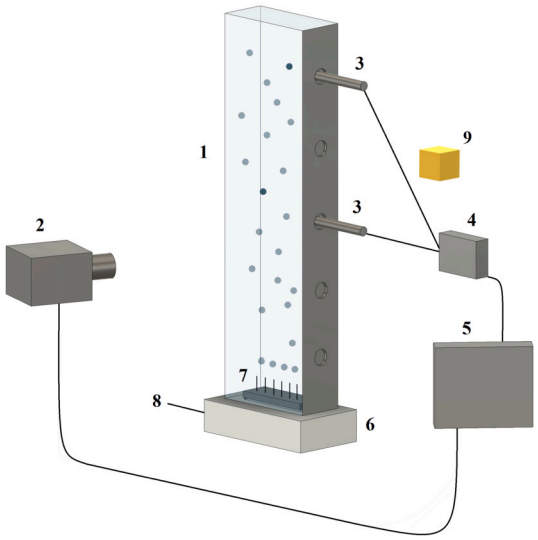

Fig. 2.1. Experimental facility composed of 1) liquid column, 2) camera, 3) oxygen probes, 4) transmitter, 5) computer, 6) gas chamber, 7) capillary bank, 8) gas supply, 9) illumination.

Table 2.1
Design parameters of the capillary banks. $D_{cap,u}$ and $D_{cap,l}$ are the inner diameter of the upper and lower capillaries, respectively. N and L are the number and length of the capillaries, respectively. ΔL_{cap} is the distance between the capillaries.

Capillary bank	$D_{cap,u}$ [mm]	$D_{cap,l}$ [mm]	N [-]	L [cm]	ΔL_{cap} [cm]
N1	1.6	0.48	16	8.9	1.2
N2	0.6	0.25	27	8.5	0.9
N3	0.13	0.13	43	7.0	0.6

Vélez-Cordero and Zenit (2011), where the inner diameters of the capillaries were selected by balancing the buoyancy and surface tension forces. The capillary bank configurations used in this work are shown in Fig. 2.2 (b-d) and the design parameters are given in Table 2.1. The geometrical ratios in Fig. 2.2 (b-d) correspond to the physical ratios. The capillaries were glued to the metal plates. For capillary banks N1 and N2, the metal plates had two sets of capillaries where the capillaries on the topside of the plates had a different inner diameter than the ones on the underside. For capillary bank N3, the inner diameter of the capillaries on the topside and underside was the same. The design of the capillary banks ensured sufficient hydrostatic resistance to produce individual bubbles and avoid the generation of gas jets. The gas volume flow rate, Q, was controlled by a flow-meter (ALICAT SCIENTIFIC MC-2slpm), and u_s was in the range of 0.07 cm/s to 0.47 cm/s ($u_s = Q/A$, where A is the cross sectional area of the bubble column). Table 2.2 provides the investigated flow conditions. All analyzes of the bubble column were conducted under ambient temperature and pressure (22 ±1 °C and 1 atm). The DO concentration was monitored by three probes (METTLER TOLEDO InPro6860i). The DO probes were inserted into the column through the side walls in such a way that they did not affect the fluid dynamics. The DO probes were inserted at two heights and on both side walls of the column to observe any effects of the measurement position. The column was disassembled and cleaned with deionized water after each experimental day. The capillary banks were cleaned after each experimental day by inserting them into a container with a water–ethanol solution. The container was then put into an ultrasonic bath and left for 20 minutes.

Data on the bubble size distribution and the mean bubble size were acquired using a high-speed camera (Photron FASTCAM MINI AX100) and a lens (Tamron SP 90mm F2.8 Di VC USD Macro), known as shadow imaging technique. The frame rate was adjusted to the desired objective; 50 frames per second (fps) when recording images for measuring the bubble size, and 500 fps when recording images for analyzing the bubble flow dynamics. The camera-to-column position was varied to obtain both high-resolution and low-resolution images, where the former were used to determine the bubble size and the latter for study of the flow fields. The camera-to-column distances were 47 cm and 147 cm for the high-resolution and the low-resolution images, respectively. Diffusion paper was attached to the column wall opposing the camera and a light-emitting diode (LED) was located 90° to the column and reflected by a panel. The resolution of the camera was 1024×1024 px^2 (pixels^2). The geometrical calibration between px and length scale was obtained as the average from the acquired images of a ruler placed in front and back of the column.

2.2. Liquid solutions

Table 2.3 summarizes the physical properties of the solutions. Deionized water and glycerol/water were used as Newtonian solutions. 0.04 M $MgSO_4$ (Magnesium sulfate heptahydrate, ACS reagent, ≥ 98%, Sigma Aldrich) was introduced in all the solutions to prevent coalescence (Lessard and Zieminski, 1971). To obtain a shear-thinning behavior with negligible elastic properties, solutions consisting of a mixture of XG, glycerol, and water were selected. The percentages of XG and glycerol solutions in Table 2.3 are given in weight terms and volume terms, respectively. The non-Newtonian solutions were prepared by dissolving XG (from Xanthomonas campestris, Sigma Aldrich) in water (preheated to 50 °C) under mechanical stirring for 60 minutes. While stirring the solution, the container was sealed with aluminum foil to keep the temperature close to 50 °C. Then the $MgSO_4$ was introduced and kept under stirring for 15 minutes. Finally, glycerol (≥ 97%, TECHNICAL, VWR Chemicals) was added. The solutions were stirred for 24 h, after which they were held at rest for additional 24 h. The resting time was necessary to let the entrapped bubbles ascend and leave the liquid.

Samples were collected each experimental day for measuring the surface tension, σ, density, ρ, and the apparent viscosity, μ_a, of the solutions. The surface tension was measured by a tensiometer (Sigma 701, Biolin Scientific, Sweden), using the Du Noüy ring method. The samples were stirred, and entrapped bubbles removed before the surface tension was measured. To measure the liquid density a density meter (DMA^{TM} 5000 M, Anton Paar GmbH, Austria) was employed. The apparent viscosity was measured by a rheometer (Physica MCR 301, Anton Paar GmbH, Austria) using a cup geometry. Before viscosity measurements, the samples were left at rest for a sufficient time to remove small bubbles trapped in the solutions. A shear rate in the range of $0.1 - 1000$ s^{-1} was applied to measure the shear-thinning behavior of the XG-solutions. The viscosity as function of shear rate is plotted in Fig. 2.3. The apparent viscosity of the non-Newtonian solutions can be characterized well with the Power-law model (Ostwald-de Waele) (Irgens, 2014):

$$\mu_a = K\dot{\gamma}^{n-1} \tag{1}$$

where K is the consistency index [Pa·s^n], n the power law index [-], and $\dot{\gamma}$ the shear rate [s^{-1}].

2.3. Volumetric mass transfer coefficient

$k_L a$ was estimated using the dynamic gas-in method (Garcia-Ochoa and Gomez, 2009). The liquid phase was flushed with nitrogen gas until the DO concentration was less than 10%. Clean compressed air was introduced, and the DO concentration was monitored until the air concentration in the liquid phase, C_L, was >70%. According to Doran (2013), the dynamics of the oxygen probe can be neglected if the probe response time, τ_p, is less than the characteristic time of mass transfer, i.e., $\tau_f = 1/(k_L a)$. The probe time constant was measured for all the probes and found negligible in all the solutions. Assuming perfect mix-

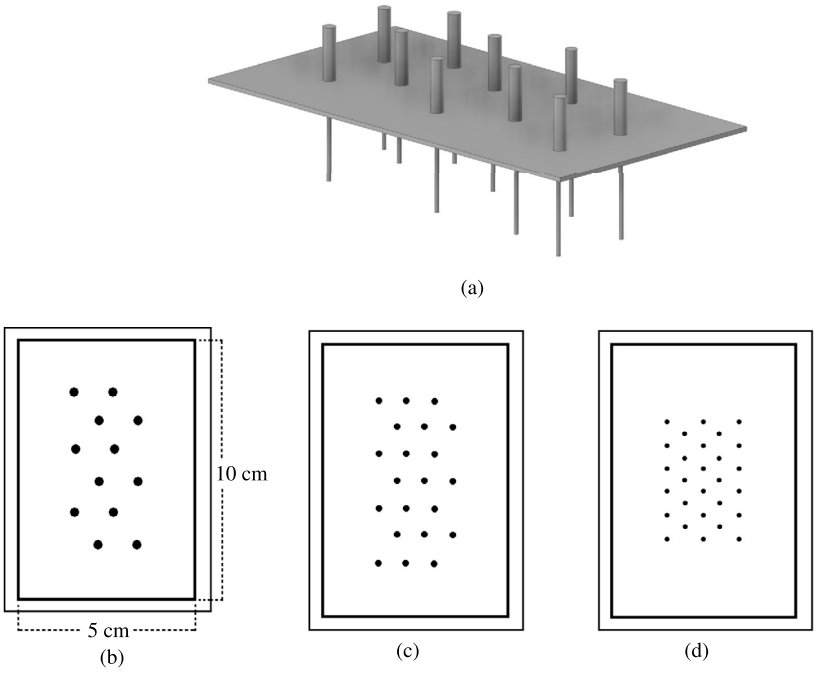

Fig. 2.2. (a) scheme of a capillary bank, and (b-d) capillary bank configurations: (b) N1, (c) N2, (d) N3.

Table 2.2
Investigated flow conditions (u_s and Q) in the liquid solutions.

	Capillary bank	Water	Glycerol/water	0.02% XG	0.1% XG
u_s	N1	[0.29, 0.4, 0.47]	[0.4, 0.47]	[0.4, 0.47]	[0.4, 0.47]
	N2	[0.07, 0.12, 0.2, 0.29, 0.4, 0.47]	[0.07, 0.29, 0.47]	[0.07, 0.47]	[0.07, 0.29, 0.47]
	N3	[0.07, 0.12, 0.2, 0.29, 0.4, 0.47]	[0.07, 0.29, 0.47]	[0.07, 0.47]	[0.07, 0.29, 0.47]
Q	N1	[0.86, 1.19, 1.42]	[1.19, 1.42]	[1.19, 1.42]	[1.19, 1.42]
	N2	[0.22, 0.35, 0.61, 0.86, 1.19, 1.42]	[0.22, 0.86, 1.42]	[0.22, 1.42]	[0.22, 0.86, 1.42]
	N3	[0.22, 0.35, 0.61, 0.86, 1.19, 1.42]	[0.22, 0.86, 1.42]	[0.22, 1.42]	[0.22, 0.86, 1.42]

Table 2.3
Physical properties of the solutions.

Solution	ρ [kg/m^3]	μ_a [mPa·s^n]	σ [mN/m]	n [-]	K [mPa·s^n]
Water	1000	1.0	72	1	-
83% glycerol/water	1226	120	63.8	1	-
0.02% XG, 75% glycerol/water	1209	...	63.2	0.856	134.2
0.1% XG, 60% glycerol/water	1173	...	64.2	0.532	411.8

ing in both phases, the rate of change of the oxygen concentration can be expressed by equation (2) as (Garcia-Ochoa and Gomez, 2009):

$$\frac{dC_L}{dt} = k_L a(C^* - C_L) \tag{2}$$

where C^* denotes the DO saturation concentration [%].

Integrating equation (2), the following linear relation is obtained:

$$\ln\left(\frac{C^* - C}{C^* - C_{t=0}}\right) = -k_L a \cdot t \tag{3}$$

where t denotes the time, and $C_{t=0}$ the DO concentration at time $t = 0$.

When the gas is switched from nitrogen to air, the incoming air mixes with the existing nitrogen until all the excess gas from the deoxygenation step is flushed out. During this process, the change of gas composition influences the measured oxygen concentration. $k_L a$ is estimated as the slope of a linear line by plotting $\ln\left(\frac{C^*-C}{C^*-C_{t=0}}\right)$ against t (in MATLAB R2021b, MathWorks, USA). $k_L a$ was estimated in the range of 30–70% oxygen concentration. The measurements were repeated three times for each operational condition. $k_L a$ was calculated as the average from the three probes applied in the set-up and for three repetitions of measurements such that an averaged $k_L a$ value for a specific bubble column condition is based on 9 independent measurements.

2.4. Bubble size and flow measurements

The number of bubbles necessary to achieve statistical significance of the bubble size data was ensured by recording a total number of 1000 images per experiment. The recorded images were processed by an image analysis algorithm using ANN, developed by SOPAT Gmbh (Berlin, Germany). The ANN algorithm was trained to recognize and distinguish between different scenarios; single bubbles, doublets, triplets, or clusters of bubbles. Further training of the algorithm is necessary for precise detection of the bubble clusters, hence, in this work the ANN algorithm has been used to determine a for bubbles that do not form part of a cluster. Fig. 2.4 illustrates the image acquisition and bubble detec-

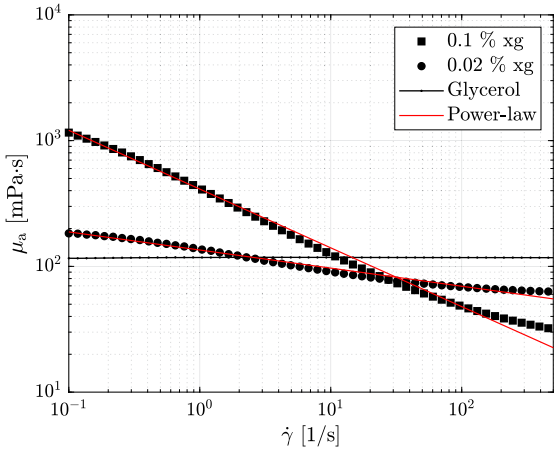

Fig. 2.3. Viscosity as function of shear rate, including the Power-law model (Irgens, 2014). The plot is presented on a logarithmic scale.

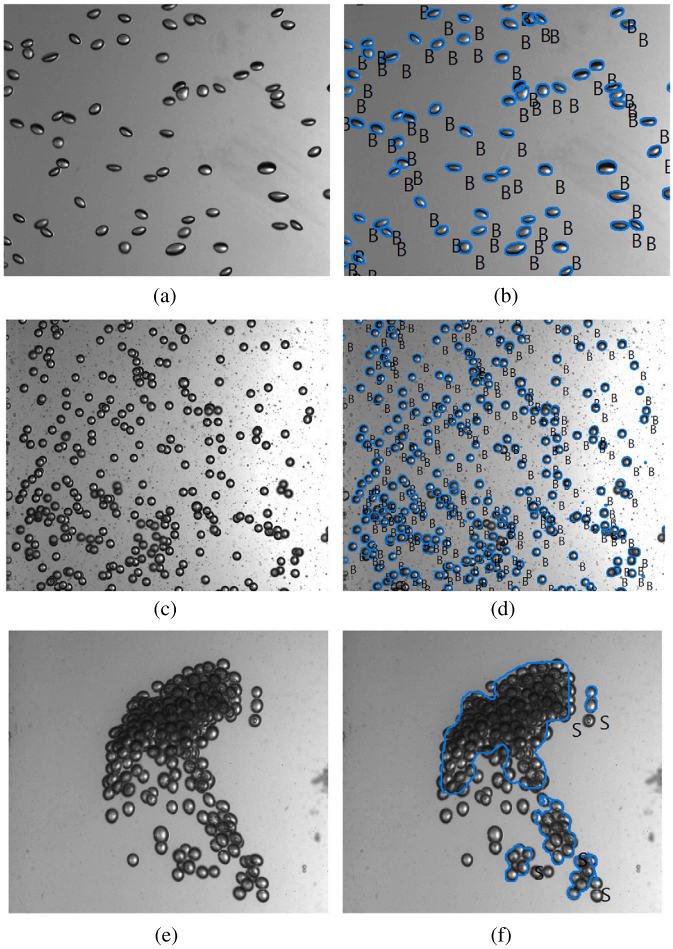

Fig. 2.4. Image acquisition and bubble detection of system (a-b) water, (c-d) glycerol/water, and (e-f) 0.1% XG. The first column shows the raw images and the second column shows the processed images. The images have been cropped and are not shown in their original sizes.

tion performed by the image analysis software. Blue borders mark the boundaries of the detected bubbles by the ANN algorithm.

In the two-dimensional plane, the Feret diameter, d_F, is based on the distance between two parallel lines that restrict a particle, in this case a bubble (Emmerich et al., 2019). Fig. 2.5 illustrates the principle of the Feret diameter using a caliper where its two parallel pins restrict

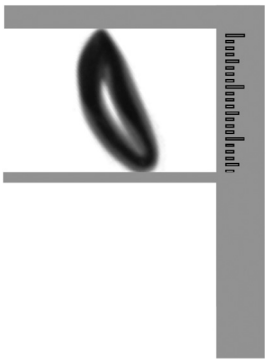

Fig. 2.5. A caliper with two parallel pins which restrict the bubble of an image.

the bubble. In such, for non-spherical bubbles, d_F depends upon the orientation of the bubble in the caliper. In the algorithm applied, 16 values of d_F are measured upon rotating the bubble in equidistantly steps between 0° and 180°. From these 16 d_F-values, the average Feret diameter, $d_{F,mean}$ is computed.

The equivalent bubble diameter, d, is estimated from $d_{F,mean}$ as:

$$d = \left(\frac{4A}{\pi}\right)^{1/2} \tag{4}$$

$$A = \frac{\pi}{4} d_{F,mean}^2 \tag{5}$$

where A denotes the side-viewed projected bubble area.

The bubbles in a bubble column are unavoidably produced with various sizes. The distribution in bubble size can be small or large depending on the sparger design, operational conditions, and fluid properties. The various bubble sizes constitute a size distribution which can be characterized in terms of a histogram. A mean bubble size is commonly computed from the bubble size distribution and applied in analyzes and calculations of mass transfer. The Sauter mean diameter, d_b, is commonly used to characterize the mean bubble size:

$$d_b = \frac{\sum_{i=1}^{N_p} d_i^3}{\sum_{i=1}^{N_p} d_i^2} \tag{6}$$

where N_p denotes the total number of bubbles, and i the bubble index number.

A sensitivity analysis was performed to evaluate the evolution of d_b versus the number of measured bubbles, n. Fig. 2.6 shows sensitivity plots for the cases of water and glycerol/water. For every new measured bubble size (blue dots), d_b was recalculated (red dots). As seen from Fig. 2.6, d_b converged rapidly for all the operational conditions (~ 5000 bubbles for water and ~ 20000 bubbles for glycerol/water were sufficient to achieve the steady bubble diameter).

2.5. Liquid mass transfer coefficient

The gas hold-up was calculated by measuring the change in liquid height due to the presence of gas. With the gas present, sufficient time was given to reach a steady state before measuring the liquid height. α_G can be related as $\alpha_G = \Delta H/H$, where H denotes the liquid level without gas ($H = 136 \pm 2$ cm in the present experiments), and ΔH the height difference resulting from the dispersed gas (Vandu et al., 2004). When d_b and α_G are known, the interfacial area can be calculated by equation (7) (Jakobsen, 2014):

$$a = \frac{6\alpha_G}{d_b} \tag{7}$$

The liquid-side mass transfer coefficient can thus be calculated by equation (8):

$$k_L = k_L a \left(\frac{6\alpha_G}{d_b}\right)^{-1} \tag{8}$$

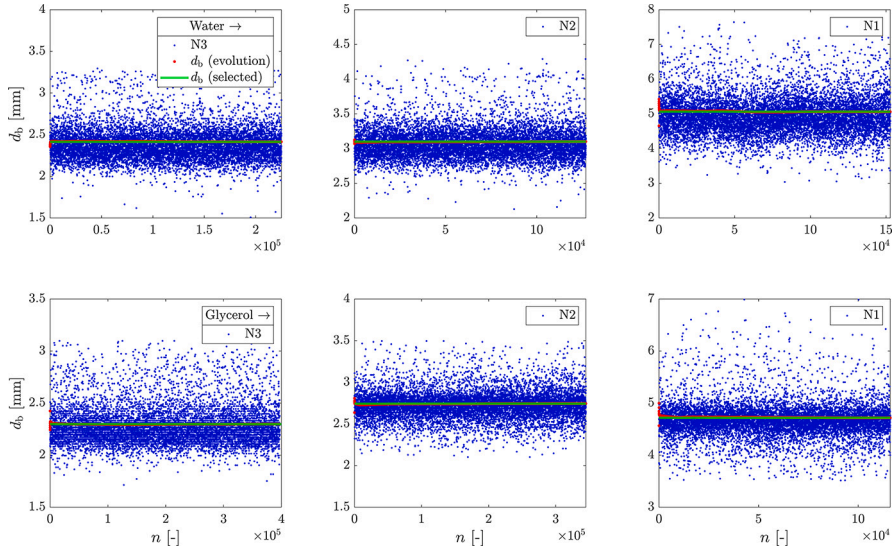

Fig. 2.6. Evolution of the calculated Sauter mean diameter (red marks) as function of the number of measured bubbles in water and glycerol/water, where $u_s = 0.07$ cm/s for capillary banks N2 and N3, and $u_s = 0.40$ cm/s for capillary bank N1. The green line marks the selected diameter.

3. Results and discussion

3.1. Bubbly flow dynamics

Figs. 3.1, 3.2, and 3.3, illustrate the bubble formation by the capillary banks in water, glycerol/water, and 0.1% XG, respectively. Fig. 3.1 shows formation of mono-sized bubbles in water by the capillary banks. Capillary banks N3 and N2 in glycerol/water (Figs. 3.2 (a-b)) and capillary bank N3 in 0.1% XG (Fig. 3.3 (a)) produce mono-sized bubbles which densely ascend in the same path close to the capillaries. In glycerol, the bubbles produced by capillary banks N3 and N2 are homogeneously dispersed across the column cross-section after approximately 20 – 30 cm. Figs. 3.4 (b) and 3.5 (b) illustrate the homogeneous dispersion in glycerol acquired at a column height of approximately 110 cm. Due to the shear-thinning behavior in 0.1% XG, a bubble produced by capillary bank N3 continues to ascend in the same path as the previous bubble along the column height. That is, a successive bubble will experience a lower viscosity and hence take this path. Fig. 3.6 illustrates the flow pattern of bubbles in the non-Newtonian solutions which ascend in the same path independent of the vertical position in the bubble column. The bubbles produced by capillary bank N1 in glycerol/water (Fig. 3.2 (c)) and capillary banks N2 and N1 in 0.1% XG (Figs. 3.3 (b-c) do not ascend in dense path close to the capillaries. In 0.1% XG, however, the bubbles produced by capillary banks N2 and N1 are affected by the shear-thinning behavior which causes the bubbles to ascend in the same path and form bubbles clusters higher up in the bubble column, as illustrated in Figs. A.1-A.3 in Appendix A.

The bubble flows are significantly different in the Newtonian and non-Newtonian solutions, as illustrated in Figs. 3.4 and 3.5, where capillary bank N3 was selected for the illustration. The bubbles in water and glycerol/water are homogeneously dispersed for all three capillary banks and at all investigated u_s in the interval of 0.07 – 0.47 cm/s. In 0.02% XG, however, the bubble flow pattern depends on the capillary bank and u_s. In 0.02% XG, capillary banks N1 and N2 produce homogeneously dispersed bubbles at all u_s. On the other hand, capillary bank N3 in 0.02% XG produces homogeneously dispersed bubbles at the highest gas velocity $u_s = 0.47$ cm/s (Fig. 3.5 (c)), while bubble clusters are formed at the lowest gas velocity $u_s = 0.07$ cm/s (Fig. 3.4 (c)). In 0.1% XG, bubble clusters are formed for all three capillary banks and at all investigated u_s; Figs. 3.4 (d) and 3.5 (d) show the bubble clusters formed by N3 at $u_s = 0.07$ cm/s and $u_s = 0.47$ cm/s, respectively. Increasing u_s in 0.1% XG leads to increased formation of single bubbles in addition to the bubble clusters, as shown by Figs. 3.4 (d) and 3.5 (d). Furthermore, an increase in u_s increases the liquid circulation where single bubbles are down-flowing on the opposite site of the uprising bubble clusters. Downflowing bubbles on opposite side of bubble clusters are illustrated for capillary bank N3 in 0.02% XG at $u_s = 0.07$ cm/s in Fig. 3.6 (b). The bubble size of the single bubbles appears to be approximately

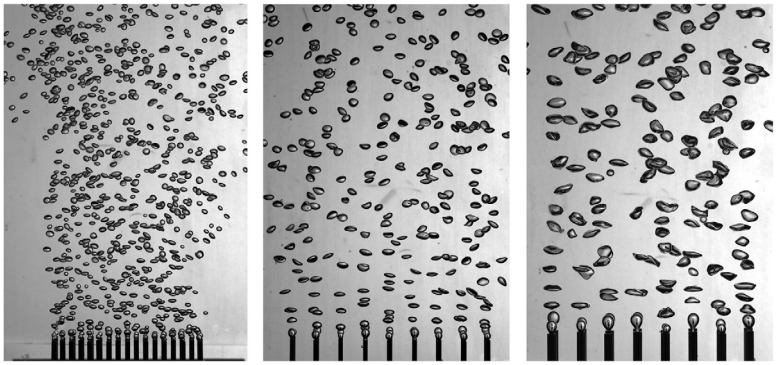

(a) (b) (c)

Fig. 3.1. Bubble formation in water by capillary bank (a) N3, (b) N2, and (c) N1, where $u_s = 0.2$ cm/s for capillary banks N2 and N3, and $u_s = 0.40$ cm/s for capillary bank N1. The images represent a physical size of (a) 11×8 cm^2, and (b-c) 12×8 cm^2.

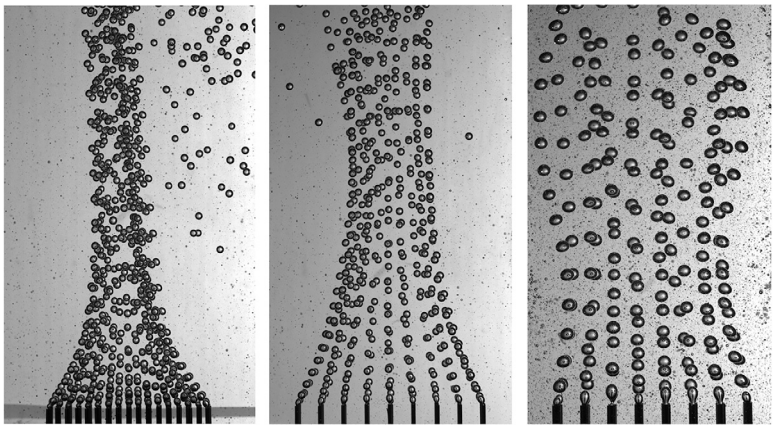

Fig. 3.2. Bubble formation in glycerol/water by capillary bank (a) N3, (b) N2, and (c) N1, where $u_s = 0.13$ cm/s for capillary banks N2 and N3, and $u_s = 0.40$ cm/s for capillary bank N1. The images represent a physical size of (a) 12×7 cm^2, and (b-c) 15×9 cm^2.

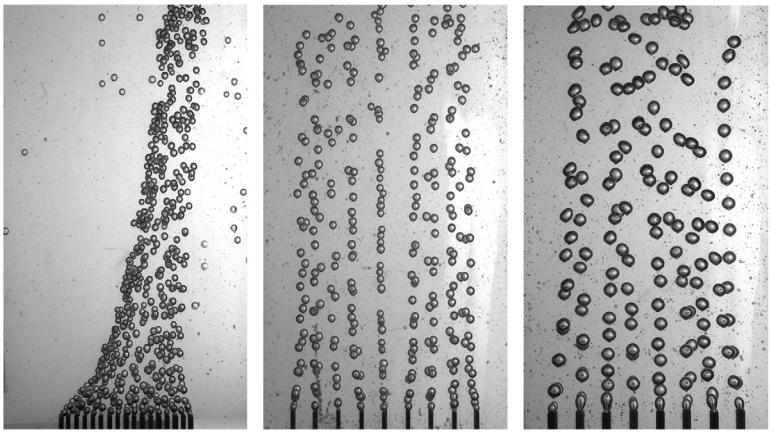

Fig. 3.3. Bubble formation in 0.1% XG by capillary bank (a) N3, (b) N2, and (c) N1, where $u_s = 0.13$ cm/s for capillary banks N2 and N3, and $u_s = 0.40$ cm/s for capillary bank N1. The images represent a physical size of 15×9 cm^2.

the same as those forming clusters. Section 3.2 presents plots of the bubble diameter of the single bubbles formed in the non-Newtonian solutions.

In 0.1% XG and 0.02% XG, a bubble takes the same path as the previous bubble released from the same capillary due to the shear-thinning effect. Fig. 3.6 illustrates the shear-thinning effect on the bubble flow field for capillary banks N2 and N3 in 0.1% XG and 0.02% XG at $u_s = 0.07$ cm/s. For capillary bank N3 at $u_s = 0.07$ cm/s in 0.1% XG (Fig. 3.6 (a)), the bubbles leaving the capillary bank are rising in the same path as the former bubbles before forming bubble clusters higher up in the column. While rising, the bubble clusters have a dynamic structure with the centered bubbles rising and the exterior bubbles descending continuously. The bubbles are changing position within the cluster as the cluster ascends, break up, and form new clusters, and hence the gas–liquid-interface is continuously renewed. Similar dynamic behavior was observed by Vélez-Cordero and Zenit (2011). The dynamic behavior of the clusters is attempted illustrated through the various cluster structures present in Fig. 3.6 (a). Comparing Figs. 3.6 (a) and (b), the bubble clusters produced by capillary bank N3 in 0.1% XG have denser structures compared to 0.02% XG, i.e., the number of bubbles forming a bubble cluster is higher and the number of single bubbles is lower in 0.1% XG. No bubble clusters are formed by capillary bank N2 at $u_s = 0.07$ cm/s in 0.02% XG (Fig. 3.6 (c)), where the bubbles ascend in a less dense path due to the design of the capillary bank. Appendix A provides additional images of the bubble clusters formed in 0.1% XG by the three capillary banks.

3.2. Sauter mean diameter

Fig. 3.7 (a) shows the influence of u_s on d_b in water. d_b produced by capillary bank N3 in water is approximately constant for $u_s \in [0.07, 0.29]$ cm/s, whereas increases with a further increase in u_s. The opposite trend is observed for capillary bank N2, where d_b increases for $u_s \in [0.07, 0.29]$ cm/s, after which d_b is constant. d_b in glycerol/water increases linearly with u_s for all the capillary banks in Fig. 3.7 (b). Capillary bank N1 produces bubbles with similar d_b in water and glycerol/water at $u_s \in [0.4, 0.47]$ cm/s. The standard deviations of d_b presented in Fig. 3.7 are minor and not visible with the scale of the figure. The uncertainties in the measurement methods, potentially resulting in systematic errors, are difficult to measure. Hence, the standard deviations of d_b, α_G, and $k_L a$ are based on the repeat of measurements.

Fig. 3.8 presents d_b for the individual bubbles (not considering the cluster size) in the non-Newtonian solutions. As in the Newtonian cases, d_b in 0.02% XG and 0.1% XG increases with an increase in u_s. d_b of the individual bubbles produced in 0.1% XG is slightly larger than that produced in glycerol/water. The bubbles produced in 0.02% XG, however, are more similar in size to those obtained in glycerol/water. Based on the trend in the data for d_b in water, glycerol/water, 0.1% XG, and 0.02% XG, it is evident that d_b is influenced by the viscosity of the solutions.

Figs. 3.9 and 3.10 show bubble size distributions at different u_s for water and glycerol/water, respectively. The bubble size distributions

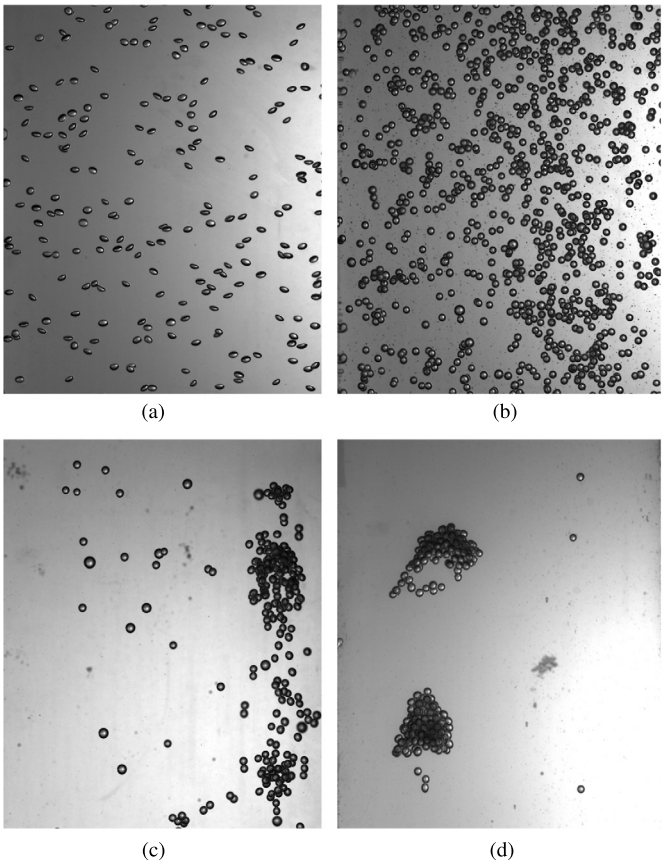

Fig. 3.4. Bubbly flow obtained with capillary bank N3 and $u_s = 0.07$ cm/s in (a) water, (b) glycerol/water, (c) 0.02% XG, and (d) 0.1% XG. The images are recorded with slightly different spatial resolutions. The images are acquired at column height of approximately 110 cm.

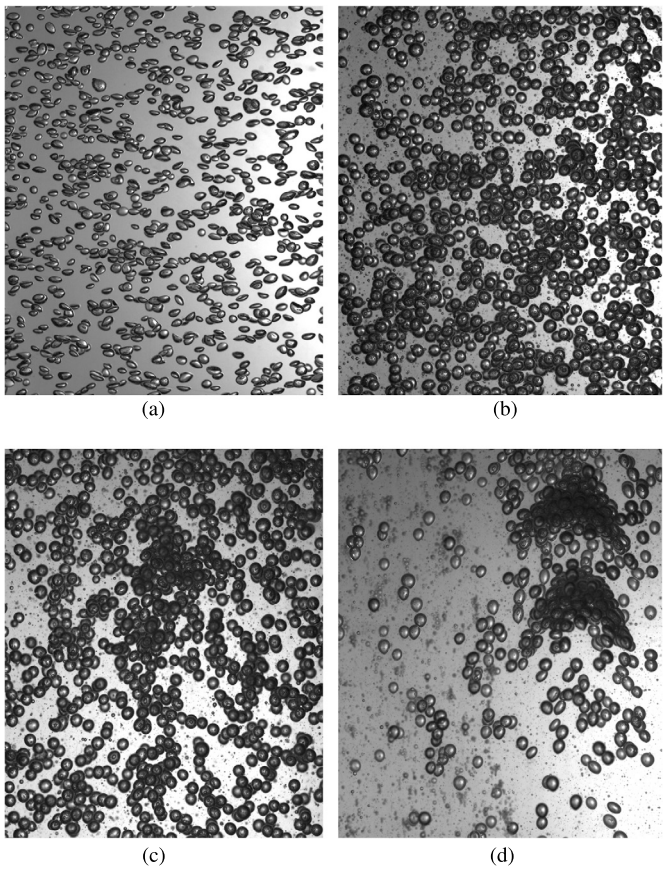

Fig. 3.5. Bubbly flow obtained with capillary bank N3 and $u_s = 0.47$ cm/s in (a) water, (b) glycerol/water, (c) 0.02% XG, and (d) 0.1% XG. The images are recorded with slightly different spatial resolutions. The images are acquired at column height of approximately 110 cm.

are distributions of d (mean Feret diameter) from which d_b (Sauter mean diameter) is calculated. The density distribution function, q, represents the number of bubbles in a defined bubble diameter class. The blue bar denotes the arithmetic mean, and the red bar the d_b of the respective bubble size distribution. As previously mentioned, a narrow bubble size distribution is desirable as it increases the certainty in the interpreted effect of a on $k_L a$. With a broad bubble size distribution, it is not possible to characterize how the various bubble sizes in the size distribution contribute to $k_L a$. Hence, having a wide bubble size distribution increases the uncertainty of the interpreted effect of a on $k_L a$.

Table 3.1 presents the maximum and minimum standard deviations of the bubble size distributions in water and glycerol/water, and the maximum and minimum number of bubbles within ±0.5 mm of the arithmetic mean in water and glycerol/water. The values presented in Table 3.1 correspond to the bubble size distributions in Figs. 3.9 and 3.10. The smallest standard deviations for capillary banks N3 and N2 in Table 3.1 are obtained for $u_s = 0.07$ cm/s in both water and glycerol/water. The smallest standard deviations for capillary bank N1 are obtained for $u_s = 0.29$ cm/s and $u_s = 0.4$ cm/s in water and glycerol/water, respectively. The standard deviations increase with an increase in u_s for all the capillary banks independent of the liquid solutions. The high percentages of bubbles within ±0.5 mm of the arithmetic means in Table 3.1 (b) give a quantitative validation of the ability of the capillary banks to produce mono-sized bubbles.

Table 3.2 provides an overview of the determined d_b in the different liquid solutions.

Table 3.1
(a) Maximum and minimum standard deviations of the bubble size distributions in water and glycerol/water for the various capillary banks and u_s, and (b) maximum and minimum number of bubbles within ±0.5 mm of the arithmetic mean in water and glycerol/water for the various capillary banks and u_s.

		Water		Glycerol/water	
		min	max	min	max
(a)	N3	9%	13%	8%	10%
	N2	7%	11%	7%	9%
	N1	10%	12%	7%	7%
(b)	N3	90%	97%	90%	98%
	N2	90%	97%	90%	99%
	N1	78%	84%	91%	93%

3.3. Gas hold-up and interfacial area

Fig. 3.11 illustrates the effect of liquid properties and u_s on α_G. Comparing the Newtonian solutions in Figs. 3.11 (a-b), α_G obtained by capillary banks N2 and N3 in glycerol/water is approximately the double of that found in water. The higher viscosity of glycerol/water increases the drag force acting on the bubbles and results in a reduced bubble rise velocity (increased residence time) and thus an increase in α_G. α_G in 0.1% XG is considerably lower than α_G in glycerol/water. This can be explained by the presence of bubble clusters which have a larger rise velocity (lower residence time) and hence reduces α_G. In 0.02% XG, bubble clusters are only obtained with capillary bank N3 at the low-

Table 3.2
d_b produced by the capillary banks in the liquid solutions.

	Capillary bank	Water	Glycerol/water	0.02% XG	0.1% XG
d_b	N1	[4.9, 5.0, 5.3]	[4.7, 4.9, 5.2]	[5.0, 5.2]	[5.5, 5.6]
	N2	[3.1, 3.2, 3.3, 3.5, 3.6]	[2.8, 3.3, 3.8]	[2.9, 4.1]	[3.3, 4.1, 4.6]
	N3	[2.4, 2.5, 2.8, 2.9]	[2.3, 3.1, 3.5]	[2.5, 3.4]	[2.7, 3.4, 3.9]

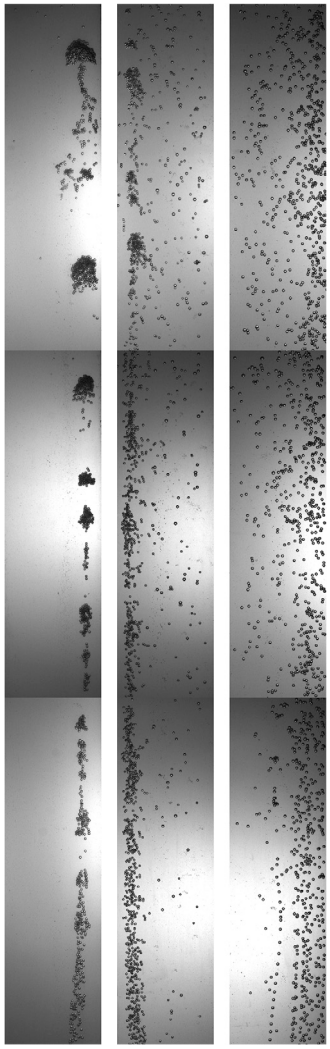

Fig. 3.6. Bubble flow field at $u_s = 0.07$ cm/s in (a) 0.1% XG using capillary bank N3, (b) 0.02% XG using capillary bank N3, and (c) 0.02% XG using capillary bank N2. The images taken in the lower-, mid-, and upper part of the bubble column have been concatenated. The column height and width presented in the images are of size 100×9 cm^2.

est u_s, where the number of bubbles constituting a cluster is lower and the number of single bubbles is higher compared to 0.1% XG. α_G is thus larger in 0.02% XG compared to 0.1% XG. α_G obtained with capillary bank N1 in glycerol/water and 0.02% XG are significantly lower than those obtained with capillary banks N2 and N3. In glycerol/water and 0.02% XG, the bubbles produced by capillary bank N1 are larger than those produced by capillary banks N2 and N3 (for the respective solutions) and thus have a larger rise velocity and lower residence time. Some coalescence is observed for capillary bank N1 in glycerol/water which leads to formation of cap bubbles. The number of cap bubbles, however, is low and the bubble flow is dominated by mono-sized bubbles.

The uncertainty in a can be calculated from the propagation of the error formula (Navidi, 2008):

$$(\delta a)^2 = \left(\frac{\partial a}{\partial \alpha_G}\delta\alpha_G\right)^2 + \left(\frac{\partial a}{\partial d_b}\delta d_b\right)^2 \tag{9}$$

$$= \left(\frac{6}{d_b}\delta\alpha_G\right)^2 + \left(\frac{-6\alpha_G}{d_b^2}\delta d_b\right)^2 \tag{10}$$

where δa denotes the uncertainty in a, $\delta\alpha_G$ the uncertainty in α_G, and δd_b the uncertainty in d_b.

Fig. 3.12 (a) shows an increase in a with an increase in u_s for all the capillary banks in water. a increases as a result of the larger increase in α_G relative to d_b with an increase in u_s. α_G obtained in water is close to equal for the capillary banks, and the largest and smallest a are therefore obtained by the smallest and largest bubbles, respectively. For capillary banks N2 and N3 in glycerol/water (Fig. 3.12 (b)), a increases with an increase in u_s, where the smallest and largest bubbles lead to higher and lower a, respectively. The low a obtained by capillary bank N1 in glycerol/water can be explained by the corresponding small α_G and large d_b. a obtained with capillary banks N2 and N3 in 0.02% XG (Fig. 3.12 (c)) is lower compared to glycerol/water due to the larger d_b and smaller α_G. The variation in d_b produced by capillary bank N1 at $u_s \in [0.4, 0.47]$ cm/s in water, glycerol/water, and 0.02% XG is within the uncertainty in d_b, and hence d_b is concluded to be independent of the solutions for the given u_s. Furthermore, α_G obtained by capillary bank N1 is equal for glycerol/water and 0.02% XG, and thus the obtained a is equal for glycerol/water and 0.02% XG.

3.4. Volumetric mass transfer coefficient

Fig. 3.13 presents k_La as a function of u_s for the different liquid solutions. In water (Fig. 3.13 (a)), k_La increases with increasing u_s for all the capillary banks. The highest k_La is obtained by capillary bank N3, producing the smallest bubbles with the largest a. By contrast, the lowest k_La is achieved with capillary bank N1, producing the largest bubbles with the smallest a. Increasing the liquid viscosity negatively affects the rate of mass transfer. As shown in Fig. 3.13, k_La obtained in water is more than a factor of ten larger than that obtained in 0.1% XG, 0.02% XG, and glycerol/water. k_La obtained in 0.02% XG and 0.1% XG is larger compared to that obtained in glycerol/water for all $u_s > 0.07$ cm/s. As it was shown in Fig. 2.3, the viscosities of 0.1% XG and 0.02% XG decrease below that of glycerol/water for $\dot{\gamma}$ of 2 s^{-1} and 10 s^{-1}, respectively. To relate the shear rate to u_s, Nishikawa et al. (1977) proposed the correlation $\dot{\gamma} = 100u_s^{1/2}$ for $u_s < 4$ cm/s and at the center of the bubble column. The correlation by Nishikawa et al. (1977) was derived based on fitting heat transfer coefficients measured in Newtonian and non-Newtonian solutions. For the u_s-values in the present study, their correlation results in $\dot{\gamma} \in [27, 67]$ s^{-1}. Schumpe and Deckwer (1987) proposed the correlation $\dot{\gamma} = 2800u_s$, which was derived based on fitting values of k_La in Newtonian and non-Newtonian solutions (e.g., XG) for $u_s > 2$ cm/s. Using the correlation by Schumpe and Deckwer (1987) for the present study results in $\dot{\gamma} \in [2, 13]$ s^{-1}. The estimations of $\dot{\gamma}$ in the present bubble column are rough estimates as the systems and operating conditions used by Nishikawa et al. (1977) and Schumpe and Deckwer (1987) are different from the present set-up. However, the estimations indicate that the viscosities of the non-Newtonian solutions are decreasing below that of glycerol/water, which reduce the resistance to mass transfer and can explain the larger values of k_La for the non-Newtonian

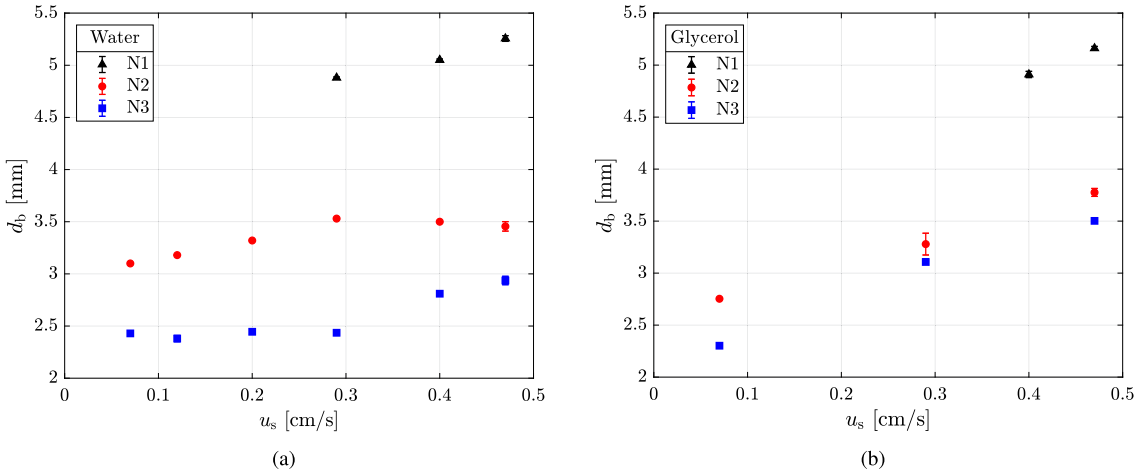

Fig. 3.7. Bubble diameter as function of superficial gas velocity in (a) water and (b) glycerol/water.

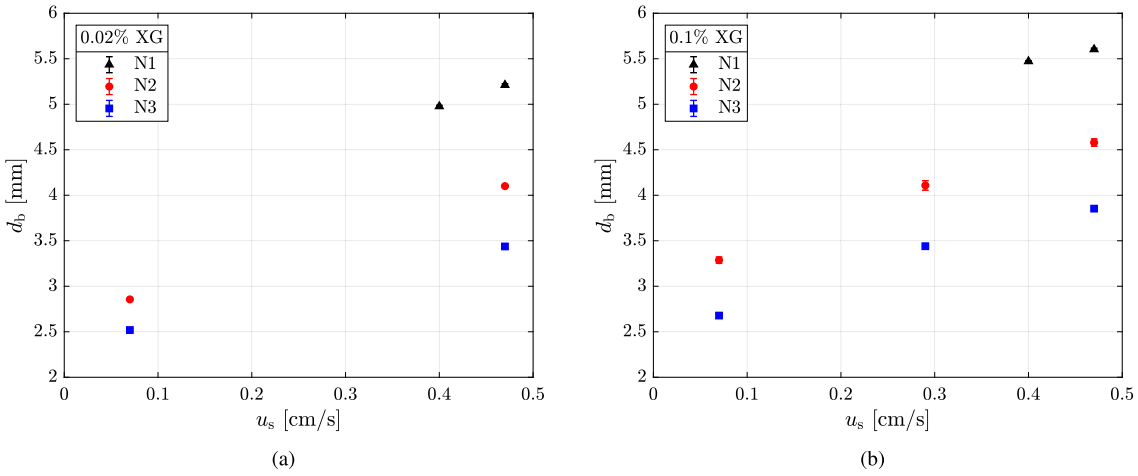

Fig. 3.8. Bubble diameter of single bubbles as function of superficial gas velocity in (a) 0.02% XG and (b) 0.1% XG.

solutions compared to glycerol/water. The rate of change of the oxygen concentration in equation (2) is calculated based on the assumption of homogeneous bubble flow. Thus, the computed $k_L a$ values in the non-Newtonian solutions are associated with larger uncertainty because the formation of bubble clusters means that the assumption of homogeneous flow is weakened.

For $u_s = 0.07$ cm/s and $u_s = 0.29$ cm/s in 0.1% XG (Fig. 3.13 (d)), the $k_L a$ achieved with capillary bank N2 is larger compared to that achieved by capillary bank N3. However, for $u_s = 0.47$ cm/s in 0.1% XG (Fig. 3.13 (d)), the $k_L a$ obtained by capillary bank N3 is larger compared to that by capillary bank N2. Increasing u_s from 0.29 cm/s to 0.47 cm/s in 0.1% XG resulted in an increase in the number of bubbles present as individual bubbles in addition to the bubble clusters. Fig. 3.8 (b) shows that the individual bubbles produced by capillary bank N3 are smaller compared to those produced by capillary bank N2. With the same α_G (Fig. 3.11 (d)), by only considering the individual bubbles in the bubble column with capillary bank N3, the measured a-value is larger compared to that obtained with capillary bank N2. This has a positive effect on $k_L a$.

The clusters were expected to negatively influence the mass transfer because many of the bubbles in a cluster are prevented from being well exposed to the surrounding liquid. However, as previously mentioned, the bubble clusters in the shear-thinning solutions are highly dynamic. That is, the interchange of bubble position and the bubble cluster collisions are observed to be highly prominent. The dynamic characteristics of the flow may have had a positive effect on the mass transfer and may explain why the mass transfer in XG was relatively high compared to the homogeneous dispersed flow in glycerol/water. At a shear rate of 2 (s^{-1}), the viscosities of 0.02% XG and 0.1% XG are approximately equal. $k_L a$ obtained in 0.1% XG is higher than that obtained in 0.02% XG. The bubble clusters are mainly formed in 0.1% XG, and hence the dynamic characteristics of the flow due to the bubble clusters may explain the larger $k_L a$ obtained in 0.1% XG compared to that obtained in 0.02% XG.

The largest standard deviations of $k_L a$ in 0.1% XG were 3%, 5%, and 4% for capillary banks N3, N2, and N1, respectively. For 0.02% XG, the largest standard deviations were 4%, 3%, and 3% for capillary banks N3, N2, and N1, respectively.

3.5. Liquid mass transfer coefficient

k_L in water is shown by Fig. 3.14 (a) to decrease with an increase in u_s. Table 3.3 provides the relative change in k_L for the capillary banks in water, glycerol/water, and 0.02% XG. The relative change in a in water is 143%, 149%, and 54% for capillary banks N3, N2, and N1, respectively. With increasing u_s in water, the decrease in k_L is much smaller than the increase in a, and the change in $k_L a$ is mainly caused by a. In glycerol/water (Fig. 3.14 (b)), k_L decreases with an increase in u_s. For capillary banks N3 and N2 in glycerol/water, k_L mainly decreases between $u_s = 0.07$ cm/s and $u_s = 0.29$ cm/s, where the relative change is 43% and 47%, respectively. Between $u_s = 0.29$ cm/s and $u_s = 0.47$ cm/s, the relative change in k_L is 14% for capillary bank N3 and 6% for capillary bank N2. The relative change in a for capillary banks N3 and N2 in glycerol/water (110% and 122%, respectively) is much larger than that

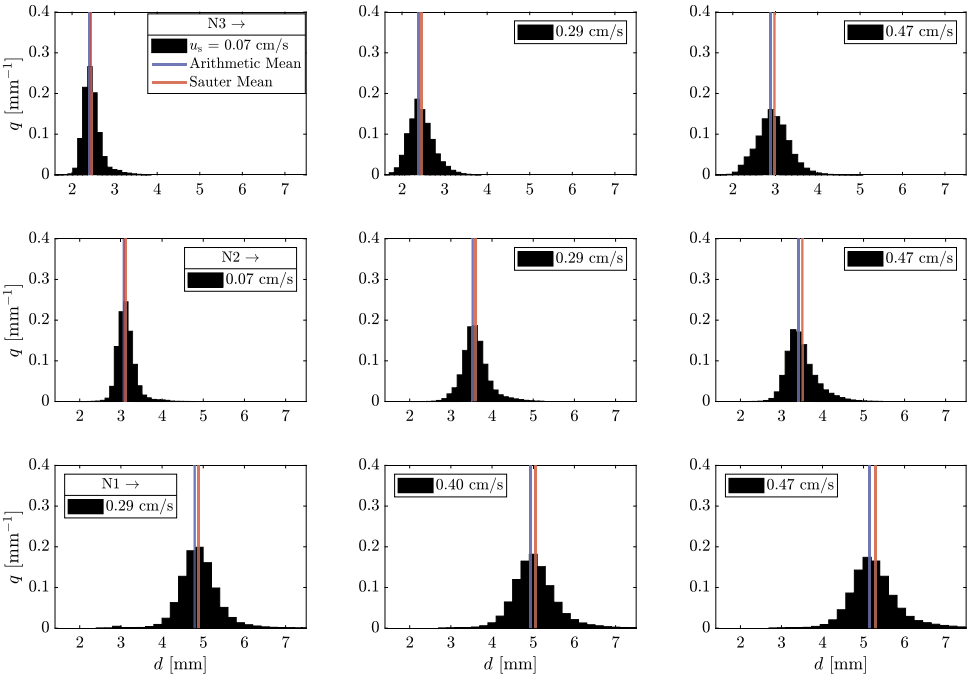

Fig. 3.9. Bubble size distributions in water where $u_s = [0.07, 0.29, 0.47]$ cm/s for capillary bank N3 (top row) and capillary bank N2 (middle row), and $u_s = [0.29, 0.4, 0.47]$ cm/s for capillary bank N1 (bottom row).

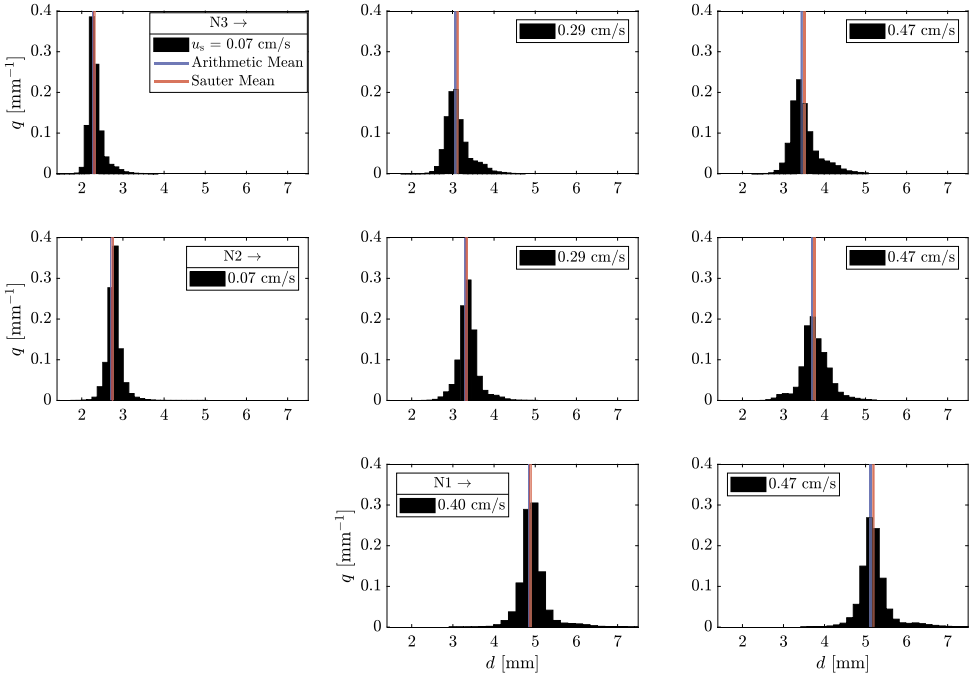

Fig. 3.10. Bubble size distributions in glycerol/water where $u_s = [0.07, 0.29, 0.47]$ cm/s for capillary bank N3 (top row) and capillary bank N2 (middle row), and $u_s = [0.4, 0.47]$ cm/s for capillary bank N1 (bottom row).

of k_L, and thus the change in $k_L a$ is mainly attributed to a. In 0.02% XG, k_L decreases with an increase in u_s for capillary banks N3 and N2. Bubble clusters are formed for capillary bank N3 at $u_s = 0.07$ cm/s and may influence the value. For capillary banks N3 and N2, the increase in a (relative change is 110% and 122%, respectively) is much larger than the decrease in k_L, and a is thus mainly causing the change in $k_L a$. For capillary bank N1 in 0.02% XG, k_L at $u_s = 0.4$ cm/s is within the standard deviation of k_L at $u_s = 0.47$ cm/s. The change in a (relative change of 9%) for capillary bank N1 in 0.02% XG causes a slight increase in $k_L a$.

The uncertainty in k_L can be calculated by the propagation of the error formula:

$$(\delta k_L)^2 = \left(\frac{\partial k_L}{\partial k_L a}\delta k_L a\right)^2 + \left(\frac{\partial k_L}{\partial a}\delta a\right)^2 \tag{11}$$

$$= \left(\frac{1}{a}\delta k_L a\right)^2 + \left(\frac{-k_L a}{a^2}\delta a\right)^2 \tag{12}$$

where δk_L denotes the uncertainty in k_L, $\delta k_L a$ the uncertainty in $k_L a$, and δa the uncertainty in a.

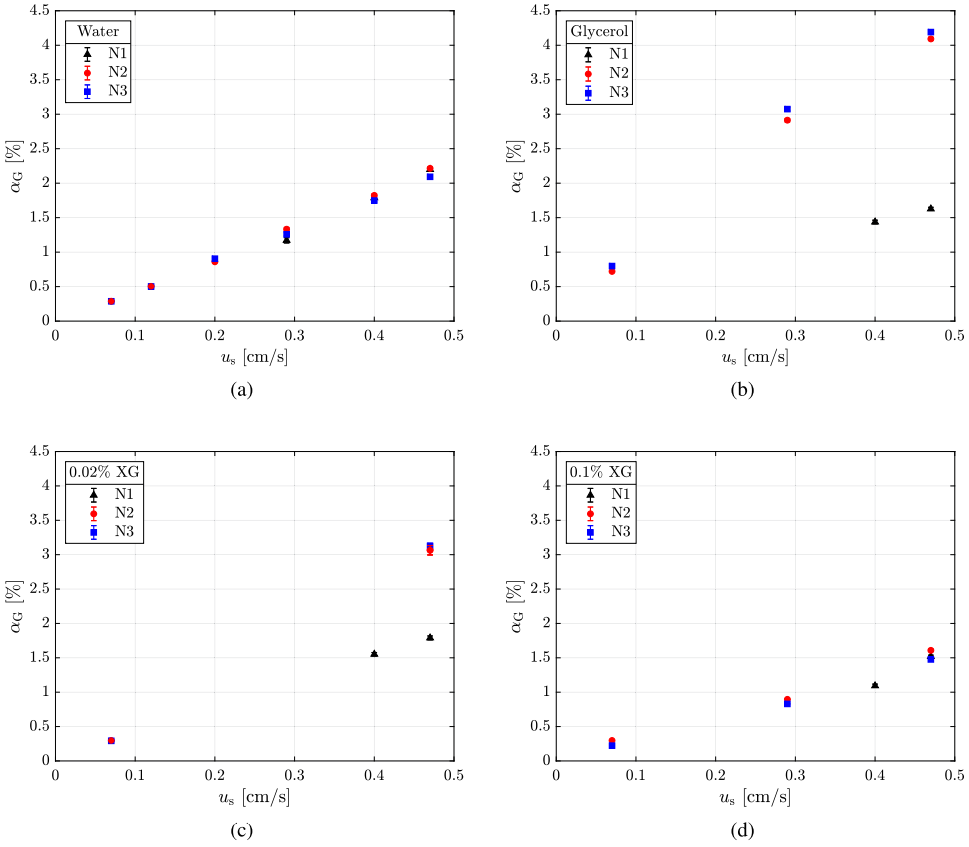

Fig. 3.11. Gas hold-up as function of superficial gas velocity in (a) water, (b) glycerol/water, (c) 0.02% XG, and (d) 0.1% XG.

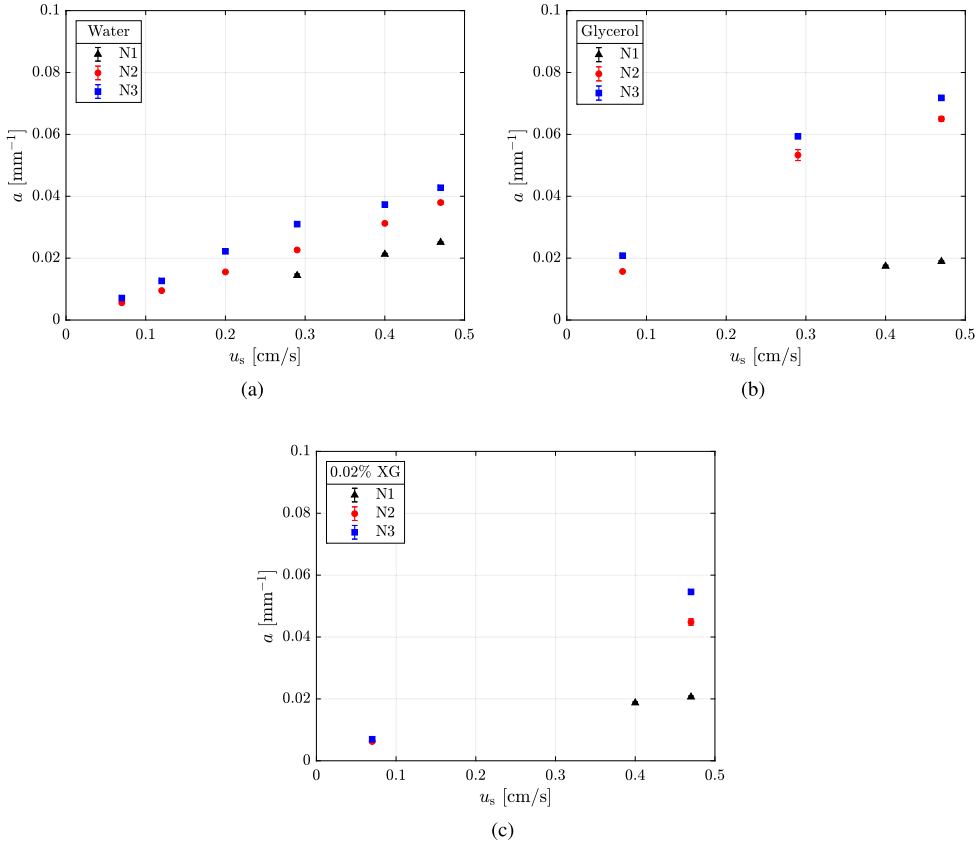

Fig. 3.12. Interfacial area as function of superficial gas velocity in (a) water, (b) glycerol/water, and (c) 0.02% XG.

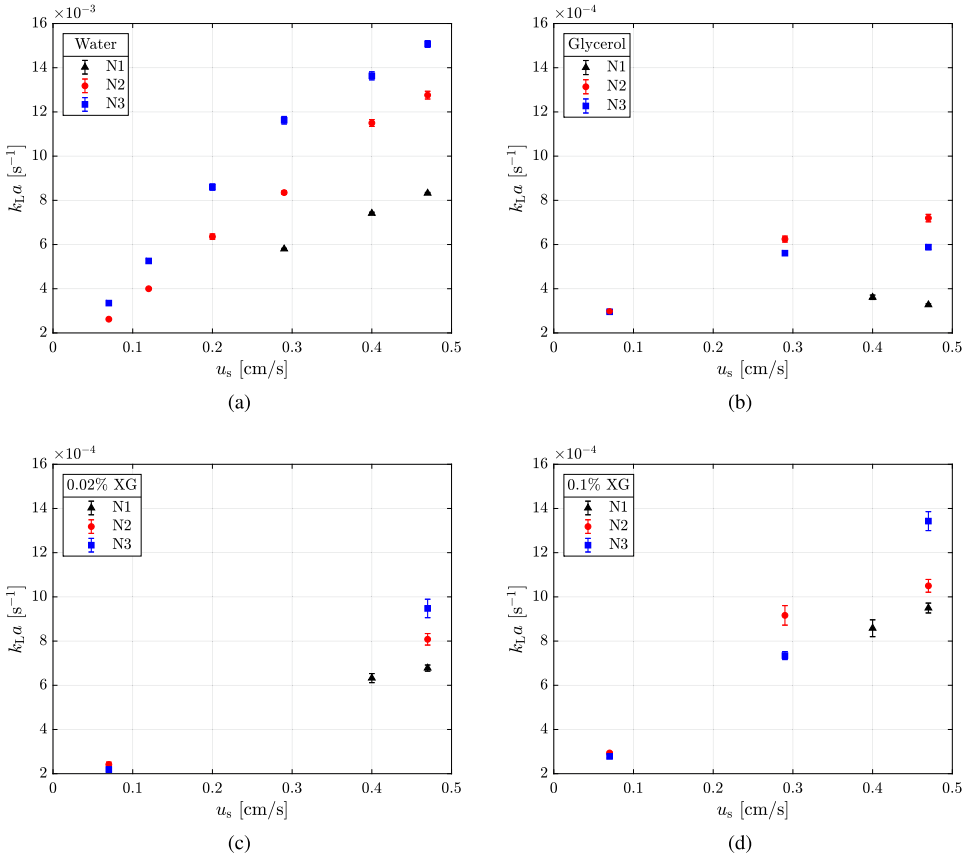

Fig. 3.13. Volumetric mass transfer coefficient as function of superficial gas velocity in (a) water, (b) glycerol/water, (c) 0.02% XG, and (d) 0.1% XG.

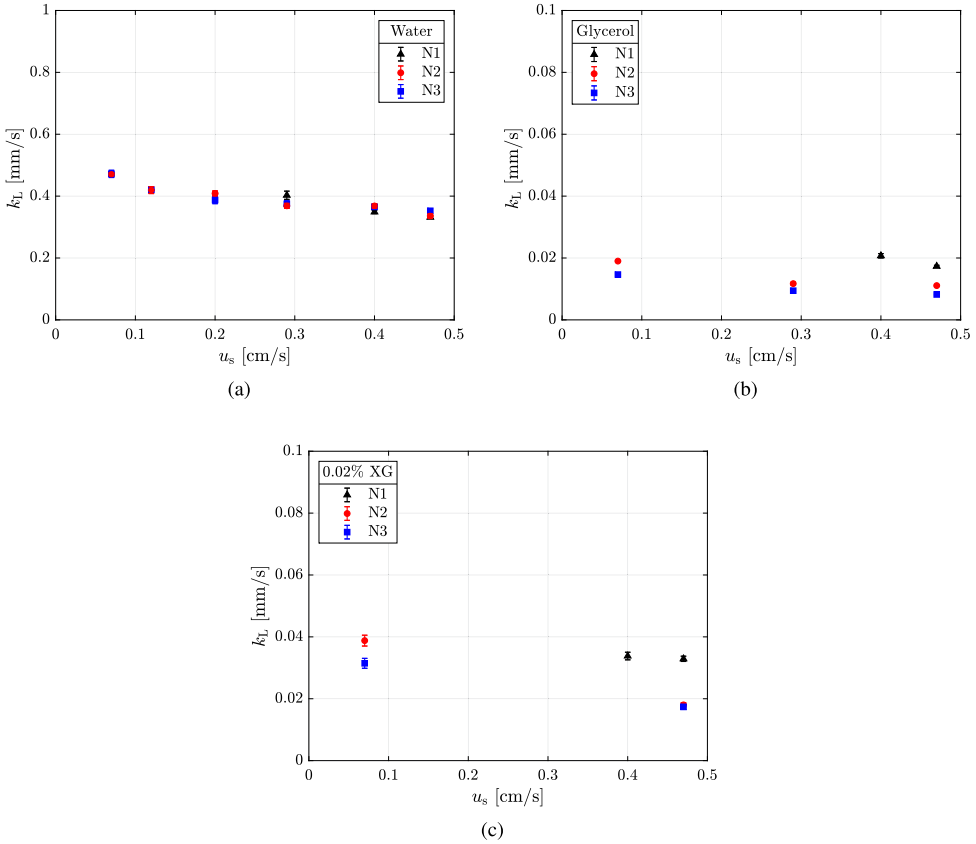

Fig. 3.14. Liquid-side mass transfer coefficient as function of superficial gas velocity in (a) water, (b) glycerol/water, and (c) 0.02% XG.

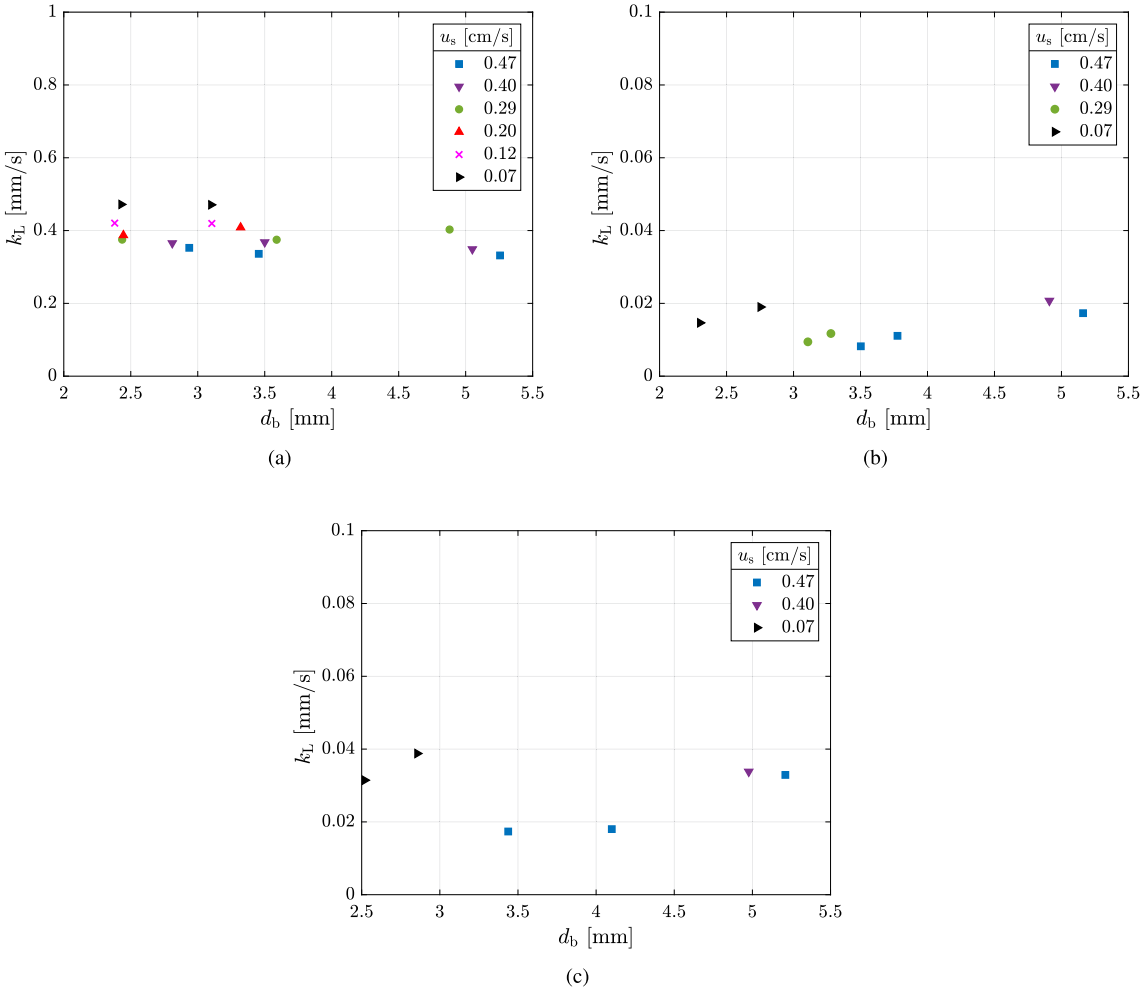

Fig. 3.15. Liquid-side mass transfer coefficient as function of bubble diameter in (a) water, (b) glycerol/water, and (c) 0.02% XG.

Table 3.3
Relative change in k_L. The relative change is here defined as $(p_{s,1} - p_{s,2})/(p_{s,1} + p_{s,2})/2$, where $p_{s,1}$ is the value of k_L at $u_s = 0.07$ cm/s for capillary banks N3 and N2, and $u_s = 0.4$ cm/s for capillary bank N1, and $p_{s,2}$ is the value of k_L at $u_s = 0.47$ cm/s.

	Water	Glycerol/water	0.02% XG
N3	29%	56%	58%
N2	33%	53%	73%
N1	19%	18%	3%

The largest standard deviations in 0.02% XG are 5% for capillary bank N3, 5% for capillary bank N2, and 4% for capillary bank N1.

k_L is shown as function of d_b in Fig. 3.15. At a given u_s in water, k_L is independent of d_b (Fig. 3.15 (a)). In glycerol/water and 0.02% XG, k_L increases with an increase in d_b at a given u_s.

4. Concluding remarks

Despite the extensive research on mass transfer in bubble columns, most of the studies are performed in Newtonian solutions, where the volumetric mass transfer coefficient k_La is determined. Only a limited number of experimental studies in Newtonian solutions exist where the individual contributions of k_L and a to k_La have been examined, and the number of studies in non-Newtonian solutions is even more limited. Motivated by industrial application such as bioprocesses, in which the fluids commonly show non-Newtonian behavior, the individual contributions of k_L and a on k_La should be further extended to viscous Newtonian and non-Newtonian solutions to increase the understanding of the complex mechanisms involved.

In this study, mass transfer and bubble hydrodynamics in Newtonian and non-Newtonian solutions were investigated in a bubble column. k_La was calculated from measurements of the local DO concentration. a was calculated based on d_b and α_G. k_L was estimated by combining k_La and a. The effects of operating conditions and liquid rheology on the mass transfer and bubble hydrodynamics were evaluated. The data from this work contributes to the experimental data necessary in developing and validating multiphase models. The main findings can be summarized as:

- The designs of the capillary banks enabled production of bubbles with a narrow bubble size distribution.

- α_G and a increased with u_s. For capillary bank N1, a was independent of the viscosity. The formation of bubble clusters reduced the residence time, hence the lowest α_G was obtained in 0.1% XG.
- $k_L a$ increased with increasing u_s and was negatively affected by the viscosity. The formation of bubble clusters did not have a prominent effect on $k_L a$. This may be explained by the highly dynamic bubble clusters of which the interchange of bubble position and cluster collisions are highly prominent. Furthermore, the dynamic flow characteristics may affect the apparent viscosity of the shear-thinning liquid in the vicinity of the bubble clusters more prominent because the bubble clusters have a higher rise velocity than small and individual bubbles. The influence of the complex dynamic flow characteristics of the bubble clusters on the mass transfer is still not fully understood, and further work on the mechanisms involved is necessary.
- The relative change in k_L was much lower than the relative change in a in water, glycerol/water, and 0.02% XG. For the investigated operational conditions and liquid solutions, the change in $k_L a$ was mainly attributed to a.
- At a given u_s, k_L was independent of d_b in water, whereas k_L increased with an increase in d_b in glycerol/water and 0.02% XG.

CRediT authorship contribution statement

Ida K. Kure: Conceptualization, Data curation, Formal analysis, Investigation, Methodology, Software, Writing – original draft. **Hugo A. Jakobsen:** Conceptualization, Supervision, Writing – review & editing. **Jannike Solsvik:** Conceptualization, Supervision, Writing – review & editing.

Declaration of competing interest

The authors declare that they have no known competing financial interests or personal relationships that could have appeared to influence the work reported in this paper.

Data availability

Data will be made available on request.

Appendix A

Figs. A.1-A.3 present different flow patterns obtained with the capillary banks, operated at various gas flow rates in 0.1% XG. The images are captured at different u_s to show the impact of the gas flow rates on the cluster shapes and formation of individual bubbles. Figs. A.1 (a-c) and A.2 (a-c) show the tendency of a horizontal orientation of the bubble clusters for $u_s = 0.07$ cm/s. When u_s increases, a vertical orientation is observed in Figs. A.1 (d-j) and A.2 (d-j) to dominate the bubble clusters. The number of individual bubbles formed in addition to the bubble clusters increases when u_s increases for all the capillary banks.

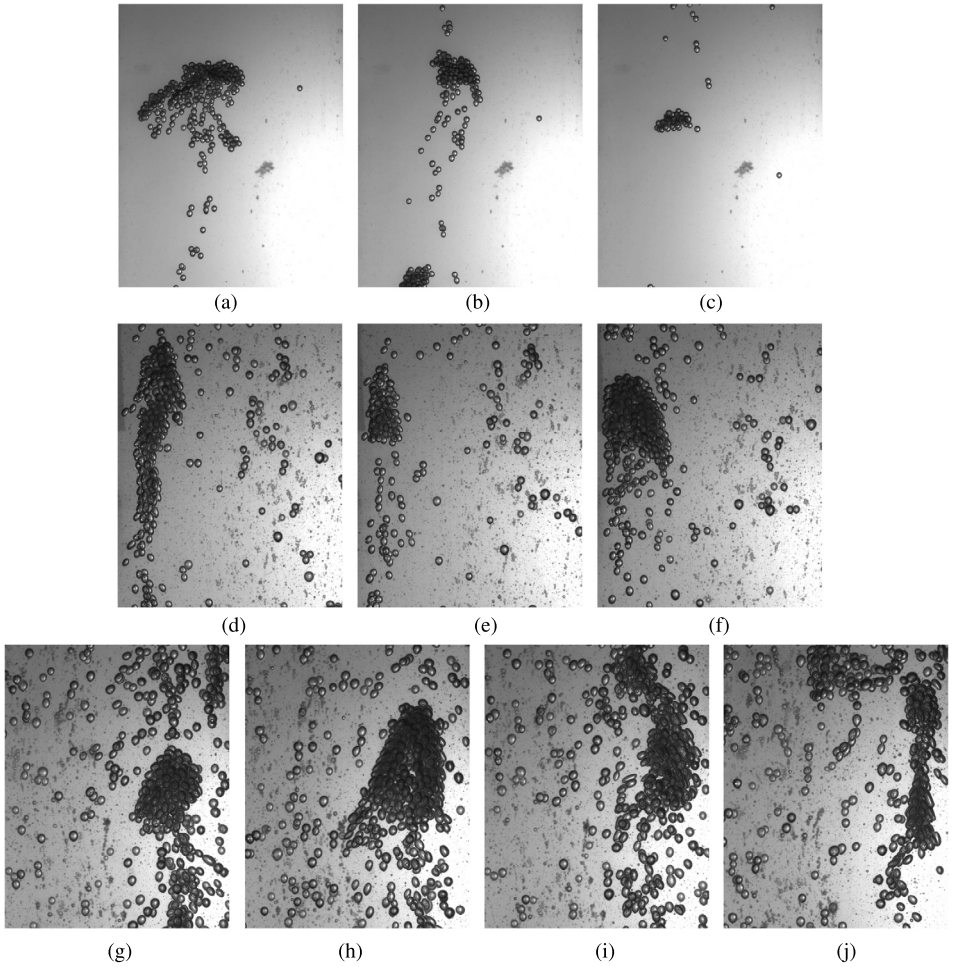

Fig. A.1. Bubble cluster shapes produced with capillary bank N3 in 0.1% XG at: (a-c) $u_s = 0.07$ cm/s, (d-f) $u_s = 0.29$ cm/s, and (g-j) $u_s = 0.47$ cm/s.

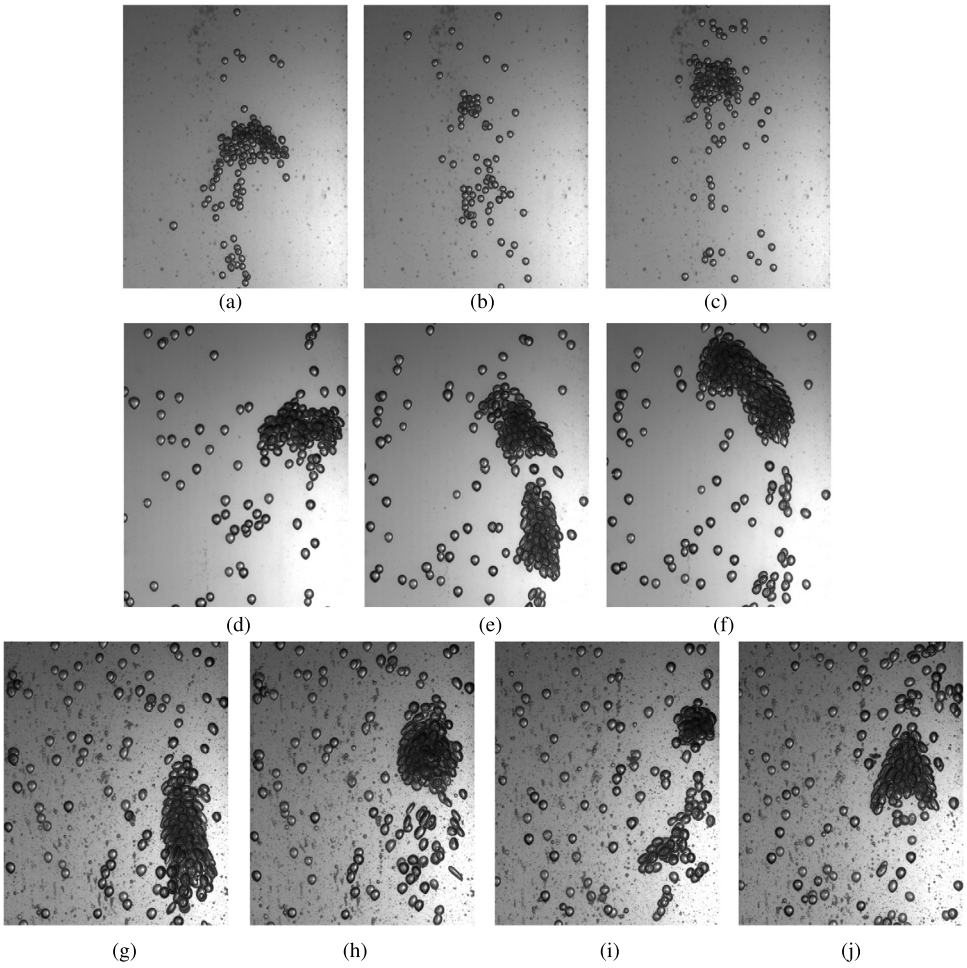

Fig. A.2. Bubble cluster shapes produced with capillary bank N2 in 0.1% XG at: (a-c) $u_s = 0.07$ cm/s, (d-f) $u_s = 0.29$ cm/s, and (g-j) $u_s = 0.47$ cm/s.

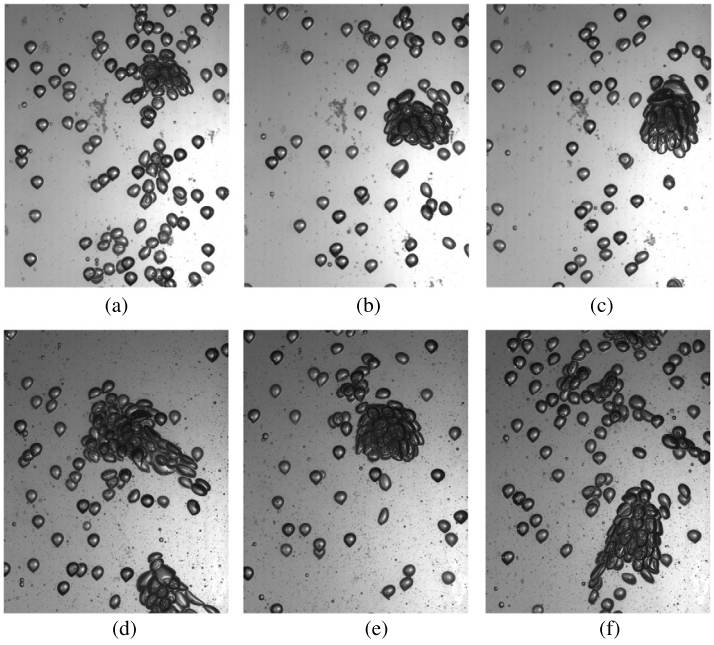

Fig. A.3. Bubble cluster shapes produced with capillary bank N1 in 0.1% XG at: (a-c) $u_s = 0.4$ cm/s, and (d-f) $u_s = 0.47$ cm/s.

References

Akita, K., Yoshida, F., 1973. Gas holdup and volumetric mass transfer coefficient in bubble columns. Ind. Eng. Chem. Process Des. Dev. 12, 76–80.

Akita, K., Yoshida, F., 1974. Bubble size, interfacial area, and liquid-phase mass transfer coefficient in bubble columns. Ind. Eng. Chem. Process Des. Dev. 13, 84–91.

Augier, F., Raimundo, P.M., 2021. Effect of rheology on mass transfer and bubble sizes in a bubble column operated in the heterogeneous regime. Can. J. Chem. Eng. 99, 1177–1185.

Badino, A., Facciotti, M., Schmidell, W., 1976. Volumetric mass transfer coefficients ($k_L a$) in batch cultivations involving non-Newtonian broths. Biotechnol. Bioeng. 18, 745–790.

Blanch, H., Bhavaraju, S., 1976. Non-Newtonian fermentation broths: rheology and mass transfer. Biotechnol. Bioeng. 18, 745–790.

Bouaifi, M., Hebrard, G., Bastoul, D., Roustan, M., 2001. A comparative study of gas hold-up, bubble size, interfacial area and mass transfer coefficients in stirred gas–liquid reactors and bubble columns. Chem. Eng. Process. 40, 97–111.

Doran, P.M., 2013. Bioprocess Engineering Principles, 2nd edition. Elsevier Ltd.

Eckenfelder Jr., W.W., Barnhart, E.L., 1961. The effect of organic substances on the transfer of oxygen from air bubbles in water. A. I. Ch. E. Journal 7, 631–634.

Emmerich, J., Tang, Q., Wang, Y., Neubauer, P., Junne, S., Maaß, S., 2019. Optical inline analysis and monitoring of particle size and shape distributions for multiple applications: scientific and industrial relevance. Chin. J. Chem. Eng. 27, 257–277.

Garcia-Ochoa, F., Gomez, E., 2009. Bioreactor scale-up and oxygen transfer rate in microbial processes: an overview. Biotechnol. Adv. 27, 153–176.

Gemello, L., Plais, C., Augier, F., Cloupet, A., Marchisio, D., 2018. Hydrodynamics and bubble size in bubble columns: effects of contaminants and spargers. Chem. Eng. Sci. 184, 93–102.

Irgens, F., 2014. Rheology and Non-Newtonian Fluids. Springer.

Jakobsen, H.A., 2014. Chemical Reactor Modeling: Multiphase Reactive Flows, 2nd ed. Springer, Berlin.

Jeng, J.J., Maa, J.R., Yang, Y.M., 1986. Surface effects and mass transfer in bubble column. Ind. Eng. Chem. Process Des. Dev. 25, 974–978.

Kawase, Y., Moo-Young, M., 1990. The effect of antifoam agents on mass transfer in bioreactors. Bioprocess Eng. 5, 169–173.

Koide, K., Yamazoe, S., Harada, S., 1985. Effects of surface-active substances on gas holdup and gas-liquid mass transfer in bubble column. J. Chem. Eng. Jpn. 18, 287–292.

Lessard, R., Zieminski, S., 1971. Bubble coalescence and gas transfer in aqueous electrolytic solutions. Ind. Eng. Chem. Fundam. 10, 260–269.

Martínez-Mercado, J., Palacios-Morales, C.A., Zenit, R., 2007. Measurement of pseudoturbulence intensity in monodispersed bubbly liquids for $10 < Re < 50$. Phys. Fluids 19.

Miller, D.N., 1983. Interfacial area, bubble coalescence and mass transfer in bubble column reactors. AIChE J. 29, 312–319.

Muroyama, K., Imai, K., Oka, Y., Hayashi, J., 2013. Mass transfer properties in a bubbles column associated with micro-bubble dispersions. Chem. Eng. Sci. 100, 464–473.

Navidi, W., 2008. Statistics for Engineers and Scientists, 2nd ed. McGraw-Hill International Edition.

Nishikawa, M., Kato, H., Hashimoto, K., 1977. Heat transfer in aerated tower filled with non-Newtonian liquid. Ind. Eng. Chem. Process Des. Dev. 16, 133–137.

Sastaravet, P., Bun, S., Wongwailikhit, K., Chawaloesphonsiya, N., Fujii, M., Painmanakul, P., 2020. Relative effect of additional solid media on bubble hydrodynamics in bubble column and airlift reactors towards mass transfer enhancement. Processes 8.

Scargiali, F., Busciglio, A., Grisafi, F., Brucato, A., 2010. Simplified dynamic pressure method for $k_L a$ measurement in aerated bioreactors. Chem. Eng. J. 49, 165–172.

Schumpe, A., Deckwer, W.-D., 1987. Viscous media in tower bioreactors: hydrodynamic characteristics and mass transfer properties. Bioprocess Eng. 2, 79–94.

Vandu, C., Koop, K., Krishna, R., 2004. Volumetric mass transfer coefficient in a slurry bubble column operating in the heterogeneous flow regime. Chem. Eng. Sci. 59, 5417–5423.

Vasconcelos, J.M.T., Rodrigues, J.M.L., Orvalho, S.C.P., Alves, S.S., Mendes, R.L., Reis, A., 2003. Effect of contaminants on mass transfer coefficients in bubble column and air lift contactors. Chem. Eng. Sci. 58, 1431–1440.

Vélez-Cordero, J.R., Zenit, R., 2011. Bubble cluster formation in shear-thinning inelastic bubbly columns. J. Non-Newton. Fluid Mech. 166, 32–41.

Vélez-Cordero, J.R., Sámano, D., Zenit, R., 2012. Study of the properties of bubbly flows in Borger-type fluids. J. Non-Newton. Fluid Mech. 175–176, 1–9.

Zednikova, M., Orvalho, S., Fialova, M., Ruzicka, M.C., 2018. Measurement of volumetric mass transfer coefficient in bubble columns. Chem. Eng. 2.